Electron and Positron Fluxes in Primary Cosmic Rays Measured with the Alpha Magnetic Spectrometer on the International Space Station

M. Aguilar,[26] D. Aisa,[33,34] A. Alvino,[33] G. Ambrosi,[33] K. Andeen,[22] L. Arruda,[24] N. Attig,[21] P. Azzarello,[33,16,†] A. Bachlechner,[1] F. Barao,[24] A. Barrau,[17] L. Barrin,[15] A. Bartoloni,[38] L. Basara,[3,37] M. Battarbee,[44] R. Battiston,[37,‡] J. Bazo,[33] U. Becker,[9] M. Behlmann,[9] B. Beischer,[1] J. Berdugo,[26] B. Bertucci,[33,34] G. Bigongiari,[35,36] V. Bindi,[19] S. Bizzaglia,[33] M. Bizzarri,[33,34] G. Boella,[28,29] W. de Boer,[22] K. Bollweg,[20] V. Bonnivard,[17] B. Borgia,[38,39] S. Borsini,[33] M. J. Boschini,[28] M. Bourquin,[16] J. Burger,[9] F. Cadoux,[16] X. D. Cai,[9] M. Capell,[9] S. Caroff,[3] J. Casaus,[26] V. Cascioli,[33] G. Castellini,[14] I. Cernuda,[26] F. Cervelli,[35] M. J. Chae,[40] Y. H. Chang,[10] A. I. Chen,[9] H. Chen,[9] G. M. Cheng,[6] H. S. Chen,[6] L. Cheng,[41] A. Chikanian,[32,*] H. Y. Chou,[10] E. Choumilov,[9] V. Choutko,[9] C. H. Chung,[1] C. Clark,[20] R. Clavero,[23] G. Coignet,[3] C. Consolandi,[19] A. Contin,[7,8] C. Corti,[19] B. Coste,[37] Z. Cui,[41] M. Dai,[5] C. Delgado,[26] S. Della Torre,[28] M. B. Demirköz,[2] L. Derome,[17] S. Di Falco,[35] L. Di Masso,[33,34] F. Dimiccoli,[37] C. Díaz,[26] P. von Doetinchem,[19] W. J. Du,[41] M. Duranti,[33] D. D'Urso,[33] A. Eline,[9] F. J. Eppling,[9] T. Eronen,[44] Y. Y. Fan,[43,§] L. Farnesini,[33] J. Feng,[3,‖] E. Fiandrini,[33,34] A. Fiasson,[3] E. Finch,[32] P. Fisher,[9] Y. Galaktionov,[9] G. Gallucci,[35,15] B. García,[26] R. García-López,[23] H. Gast,[1] I. Gebauer,[22] M. Gervasi,[28,29] A. Ghelfi,[17] W. Gillard,[10] F. Giovacchini,[26] P. Goglov,[9] J. Gong,[31] C. Goy,[3] V. Grabski,[27] D. Grandi,[28] M. Graziani,[33,15] C. Guandalini,[7,8] I. Guerri,[35,36] K. H. Guo,[18] M. Habiby,[16] S. Haino,[10,43] K. C. Han,[25] Z. H. He,[18] M. Heil,[22,9] J. Hoffman,[10] T. H. Hsieh,[9] Z. C. Huang,[18] C. Huh,[13] M. Incagli,[35] M. Ionica,[33] W. Y. Jang,[13] H. Jinchi,[25] K. Kanishev,[37] G. N. Kim,[13] K. S. Kim,[13] Th. Kirn,[1] R. Kossakowski,[3] O. Kounina,[9] A. Kounine,[9] V. Koutsenko,[9] M. S. Krafczyk,[9] S. Kunz,[22] G. La Vacca,[28,15] E. Laudi,[33,34,¶] G. Laurenti,[7,8] I. Lazzizzera,[37] A. Lebedev,[9] H. T. Lee,[43] S. C. Lee,[43] C. Leluc,[16] H. L. Li,[43,**] J. Q. Li,[31] Q. Li,[31] Q. Li,[9,††] T. X. Li,[18] W. Li,[4] Y. Li,[16,‖] Z. H. Li,[6] Z. Y. Li,[43,‖] S. Lim,[40] C. H. Lin,[43] P. Lipari,[38] T. Lippert,[21] D. Liu,[43] H. Liu,[31] T. Lomtadze,[35] M. J. Lu,[37,‡‡] Y. S. Lu,[6] K. Luebelsmeyer,[1] F. Luo,[41] J. Z. Luo,[31] S. S. Lv,[18] R. Majka,[32] A. Malinin,[12] C. Mañá,[26] J. Marín,[26] T. Martin,[20] G. Martínez,[26] N. Masi,[7,8] D. Maurin,[17] A. Menchaca-Rocha,[27] Q. Meng,[31] D. C. Mo,[18] L. Morescalchi,[35,§§] P. Mott,[20] M. Müller,[1] J. Q. Ni,[18] N. Nikonov,[22] F. Nozzoli,[33] P. Nunes,[24] A. Obermeier,[1] A. Oliva,[26] M. Orcinha,[24] F. Palmonari,[7,8] C. Palomares,[26] M. Paniccia,[16] A. Papi,[33,34] E. Pedreschi,[35] S. Pensotti,[28,29] R. Pereira,[24,19] F. Pilo,[35] A. Piluso,[33,34] C. Pizzolotto,[33] V. Plyaskin,[9] M. Pohl,[16] V. Poireau,[3] E. Postaci,[2] A. Putze,[3] L. Quadrani,[7,8] X. M. Qi,[18] P. G. Rancoita,[28] D. Rapin,[16] J. S. Ricol,[17] I. Rodríguez,[26] S. Rosier-Lees,[3] A. Rozhkov,[9] D. Rozza,[28] R. Sagdeev,[11] J. Sandweiss,[32] P. Saouter,[16] C. Sbarra,[7,8] S. Schael,[1] S. M. Schmidt,[21] D. Schuckardt,[22] A. Schulz von Dratzig,[1] G. Schwering,[1] G. Scolieri,[33] E. S. Seo,[12] B. S. Shan,[4] Y. H. Shan,[4] J. Y. Shi,[31] X. Y. Shi,[9,‖‖] Y. M. Shi,[42] T. Siedenburg,[1] D. Son,[13] F. Spada,[38] F. Spinella,[35] W. Sun,[9] W. H. Sun,[9,¶¶] M. Tacconi,[28,29] C. P. Tang,[18] X. W. Tang,[6] Z. C. Tang,[6] L. Tao,[3] D. Tescaro,[23] Samuel C. C. Ting,[9] S. M. Ting,[9] N. Tomassetti,[17] J. Torsti,[44] C. Türkoğlu,[2] T. Urban,[20] V. Vagelli,[22] E. Valente,[38,39] C. Vannini,[35] E. Valtonen,[44] S. Vaurynovich,[9] M. Vecchi,[3] M. Velasco,[26] J. P. Vialle,[3] L. Q. Wang,[41] Q. L. Wang,[5] R. S. Wang,[42] X. Wang,[9] Z. X. Wang,[18] Z. L. Weng,[9] K. Whitman,[19] J. Wienkenhöver,[1] H. Wu,[31] X. Xia,[26,**] M. Xie,[9,††] S. Xie,[42] R. Q. Xiong,[31] G. M. Xin,[41] N. S. Xu,[18] W. Xu,[6,9] Q. Yan,[6] J. Yang,[40] M. Yang,[6] Q. H. Ye,[42] H. Yi,[31] Y. J. Yu,[5] Z. Q. Yu,[6] S. Zeissler,[22] J. H. Zhang,[31] M. T. Zhang,[18] X. B. Zhang,[18] Z. Zhang,[18] Z. M. Zheng,[4] H. L. Zhuang,[6] V. Zhukov,[1] A. Zichichi,[7,8] N. Zimmermann,[1] P. Zuccon,[9] and C. Zurbach[30]

(AMS Collaboration)

[1]*I. Physics Institute and JARA-FAME, RWTH Aachen University, D-52056 Aachen, Germany*
[2]*Department of Physics, Middle East Technical University (METU), 06800 Ankara, Turkey*
[3]*Laboratoire d'Annecy-Le-Vieux de Physique des Particules (LAPP), IN2P3/CNRS and Université de Savoie, F–74941 Annecy-le-Vieux, France*
[4]*Beihang University (BUAA), Beijing 100191, China*
[5]*Institute of Electrical Engineering (IEE), Chinese Academy of Sciences, Beijing 100080, China*
[6]*Institute of High Energy Physics (IHEP), Chinese Academy of Sciences, Beijing, 100039, China*
[7]*INFN-Sezione di Bologna, I-40126 Bologna, Italy*
[8]*Università di Bologna, I-40126 Bologna, Italy*
[9]*Massachusetts Institute of Technology (MIT), Cambridge, Massachusetts 02139, USA*
[10]*National Central University (NCU), Chung-Li, Tao Yuan 32054, Taiwan*
[11]*East-West Center for Space Science, University of Maryland, College Park, Maryland 20742, USA*
[12]*IPST, University of Maryland, College Park, Maryland 20742, USA*

[13]CHEP, Kyungpook National University, 702-701 Daegu, Korea
[14]CNR-IROE, I-50125 Firenze, Italy
[15]European Organization for Nuclear Research, CERN, CH-1211 Geneva 23, Switzerland
[16]DPNC, Université de Genève, CH-1211 Genève 4, Switzerland
[17]Laboratoire de Physique subatomique et de cosmologie (LPSC), Université Grenoble-Alpes, CNRS/IN2P3, F-38026 Grenoble, France
[18]Sun Yat-Sen University, SYSU, Guangzhou 510275, China
[19]University of Hawaii, Physics and Astronomy Department, 2505 Correa Road, WAT 432, Honolulu, Hawaii 96822, USA
[20]National Aeronautics and Space Administration (NASA), Johnson Space Center and Jacobs-Sverdrup, Houston, Texas 77058, USA
[21]Jülich Supercomputing Centre and JARA-FAME, Research Centre Jülich, D-52425 Jülich, Germany
[22]Institut für Experimentelle Kernphysik, Karlsruhe Institute of Technology (KIT), D-76128 Karlsruhe, Germany
[23]Instituto de Astrofísica de Canarias (IAC), E-38205 La Laguna, Tenerife, Spain
[24]Laboratório de Instrumentação e Física Experimental de Partículas, LIP, P-1000 Lisboa, Portugal
[25]National Chung-Shan Institute of Science and Technology (NCSIST), Longtan, Tao Yuan 325, Taiwan
[26]Centro de Investigaciones Energéticas, Medioambientales y Tecnológicas (CIEMAT), E-28040 Madrid, Spain
[27]Instituto de Física, Universidad Nacional Autónoma de México (UNAM), México, D.F., 01000 México
[28]INFN-Sezione di Milano-Bicocca, I-20126 Milano, Italy
[29]Università di Milano-Bicocca, I-20126 Milano, Italy
[30]Laboratoire Univers et Particules de Montpellier (LUPM), IN2P3/CNRS and Université de Montpellier II, F-34095 Montpellier, France
[31]Southeast University, SEU, Nanjing 210096, China
[32]Physics Department, Yale University, New Haven, Connecticut 06520, USA
[33]INFN-Sezione di Perugia, I-06100 Perugia, Italy
[34]Università di Perugia, I-06100 Perugia, Italy
[35]INFN-Sezione di Pisa, I-56100 Pisa, Italy
[36]Università di Pisa, I-56100 Pisa, Italy
[37]INFN–TIFPA and Università di Trento, I-38123 Povo, Trento, Italy
[38]INFN-Sezione di Roma 1, I-00185 Roma, Italy
[39]Università di Roma La Sapienza, I-00185 Roma, Italy
[40]Department of Physics, Ewha Womans University, Seoul 120-750, Korea
[41]Shandong University, SDU, Jinan, Shandong 250100, China
[42]Shanghai Jiaotong University (SJTU), Shanghai 200030, China
[43]Institute of Physics, Academia Sinica, Nankang, Taipei 11529, Taiwan
[44]Space Research Laboratory, Department of Physics and Astronomy, University of Turku, FI-20014 Turku, Finland

(Received 12 August 2014; revised manuscript received 26 August 2014; published 18 September 2014)

Precision measurements by the Alpha Magnetic Spectrometer on the International Space Station of the primary cosmic-ray electron flux in the range 0.5 to 700 GeV and the positron flux in the range 0.5 to 500 GeV are presented. The electron flux and the positron flux each require a description beyond a single power-law spectrum. Both the electron flux and the positron flux change their behavior at ~30 GeV but the fluxes are significantly different in their magnitude and energy dependence. Between 20 and 200 GeV the positron spectral index is significantly harder than the electron spectral index. The determination of the differing behavior of the spectral indices versus energy is a new observation and provides important information on the origins of cosmic-ray electrons and positrons.

DOI: 10.1103/PhysRevLett.113.121102 PACS numbers: 96.50.sb, 95.35.+d, 95.85.Ry, 98.70.Sa

Measurements of the electron flux and the positron flux in primary cosmic rays with the Alpha Magnetic Spectrometer (AMS) on the International Space Station (ISS) are presented. The measurements are based on 41×10^9 events collected between May 19, 2011, and November 26, 2013, and cover the energy ranges 0.5 to 700 GeV for electrons and 0.5 to 500 GeV for positrons.

AMS has measured the positron fraction, $\Phi_{e^+}/(\Phi_{e^+} + \Phi_{e^-})$, as a function of energy from 0.5 to 350 GeV, where Φ_{e^+} is the flux of positrons and Φ_{e^-} is the flux of electrons. The fraction was found to be steadily increasing from 10 to ~250 GeV, but from 20 to 250 GeV the slope decreases by an order of magnitude [1]. The latest results from AMS, based on a factor 1.7 increase in statistics, extend the energy range of the previous observation to 500 GeV and increase its precision. They show that above ~200 GeV the positron fraction no longer increases with energy [2]. The results from AMS on the positron fraction generated widespread interest and discussions on the origin of high-energy positrons [3]. Precise measurements of the

individual electron and positron fluxes as a function of energy provide insight into the origin of cosmic rays.

AMS detector.—The AMS detector [1,4] consists of a permanent magnet, nine planes of precision silicon tracker, a transition radiation detector (TRD), four planes of time-of-flight (TOF) counters, an array of anticoincidence counters, a ring imaging Čerenkov detector, and an electromagnetic calorimeter (ECAL). AMS operates continuously on the ISS and is monitored and controlled around the clock from the ground. The timing, location, and attitude are determined by a combination of GPS units affixed to AMS and to the ISS.

The tracker accurately determines the trajectory, momentum p, charge $|Z|$, and charge sign of cosmic rays by multiple measurements of the coordinates and energy loss. The coordinate resolution of each plane is measured to be better than 10 μm in the bending direction and the charge resolution is $\Delta Z \approx 0.06$ for $|Z| = 1$ particles. The maximum detectable rigidity ($|p/Z|$) of the tracker is 2 TV over a lever arm of 3 m.

To differentiate between $e^{\pm}$ and protons in the TRD, this analysis uses a TRD likelihood formed from the product of the log-likelihood probabilities of the $e^{\pm}$ hypothesis from the signals of the 20 layers of proportional tubes.

Signals from the 17 radiation length ECAL are scaled to provide the incoming (top of AMS) energy E of electrons and positrons. In the beam tests of the AMS detector, the energy resolution has been measured to be $\sigma(E)/E = \sqrt{(0.104)^2/E + (0.014)^2}$ (E in GeV). The three-dimensional shower shape is described by an ECAL estimator based on a boosted decision tree algorithm [5], and this is used to separate $e^{\pm}$ from protons independently from the TRD.

The entire detector has been extensively calibrated in a test beam at CERN with e^+ and e^- from 10 to 290 GeV/c, with protons at 180 and 400 GeV/c, and with $\pi^{\pm}$ from 10 to 180 GeV/c, which produce transition radiation equivalent to protons up to 1.2 TeV/c. Measurements with 18 different energies and particles at 2000 positions were performed. A Monte Carlo program based on the GEANT 4.9.4 package [6] is used to simulate physics processes and signals in the detector. The detector performance is steady over time.

Data analysis.—The isotropic fluxes of cosmic-ray electrons and positrons in the energy bin E of width ΔE are given by

$$\Phi_{e^{\pm}}(E) = \frac{N_{e^{\pm}}(E)}{A_{\mathrm{eff}}(E)\epsilon_{\mathrm{trig}}(E)T(E)\Delta E}, \quad (1)$$

where N_{e^-} is the number of electrons, N_{e^+} is the number of positrons, A_{eff} is the effective acceptance, ϵ_{trig} is the trigger efficiency, and T is the exposure time. The effective acceptance is defined as

$$A_{\mathrm{eff}} = A_{\mathrm{geom}}\epsilon_{\mathrm{sel}}\epsilon_{\mathrm{id}}(1+\delta), \quad (2)$$

where A_{geom} is the geometric acceptance, ϵ_{sel} is the selection efficiency, ϵ_{id} is the identification efficiency for electrons or positrons, and δ is a minor correction described below.

The geometric acceptance for this analysis is $A_{\mathrm{geom}} \simeq 550$ cm^2 sr. The product $A_{\mathrm{geom}}\epsilon_{\mathrm{sel}}\epsilon_{\mathrm{id}}$ is determined from Monte Carlo simulation.

The trigger efficiency ϵ_{trig} is determined from data. The data acquisition system is triggered by the coincidence of all four TOF planes. AMS also records unbiased triggers that require a coincidence of any three out of the four TOF planes to measure ϵ_{trig}. It is found to be 100% above 3 GeV decreasing to 75% at 1 GeV.

The exposure time as a function of energy $T(E)$ is determined by counting the live time weighted number of seconds at each location where the geomagnetic cutoff requirement, see below, is satisfied. $T(E)$ does not include the time during TRD gas refills, time spent in the South Atlantic Anomaly, and time when the AMS z axis was more than 40° from the local zenith due to ISS operations. The exposure time for this analysis at 5 GeV is 1.4×10^7 s, at 10 GeV it is 3.2×10^7 s, and above 30 GeV it is constant at 6.1×10^7 s.

The absolute energy scale is verified by using minimum ionizing particles and the ratio E/p. These results are compared with the test beam values where the beam energy is known to high precision. This comparison limits the uncertainty of the absolute energy scale to 2% in the range covered by the beam test results, 10–290 GeV. Below 10 GeV it increases to 5% at 0.5 GeV and above 290 GeV to 4% at 700 GeV. This is treated as an uncertainty of the bin boundaries. The bin widths ΔE are chosen to be at least 2 times the energy resolution to minimize migration effects. The bin-to-bin migration error is ~1% at 1 GeV; it decreases to 0.2% above 10 GeV. With increasing energy the bin width becomes smoothly wider to ensure adequate statistics in each bin.

Events are selected by requiring the presence of a shower in the ECAL and a reconstructed track in the TRD and in the tracker. To identify downward-going particles of charge $|Z| = 1$, cuts are applied on the velocity measured by the TOF and on the charge reconstructed by the tracker, the upper TOF planes, and the TRD. To reject positrons and electrons produced by the interaction of primary cosmic rays with the atmosphere, the minimum energy within the bin is required to exceed 1.2 times the Størmer cutoff [7] for either a positron or an electron at the geomagnetic location where the particle was detected and at any angle within the acceptance. The selection efficiency ϵ_{sel} is determined from the Monte Carlo simulation and found to be a smooth function of energy with a value of ~70% at 100 GeV.

The identification of the e^- and e^+ signal requires rejection of the proton background. Cuts are applied on the E/p matching and the reconstructed depth of the shower maximum. This makes the negatively charged

sample, as determined by the rigidity, a sample of pure electrons. A cut on the ECAL estimator is applied to further reduce the proton background in the positive rigidity sample after which the numbers of positrons and protons are comparable at all energies. The identification efficiency ϵ_{id} is defined using the Monte Carlo simulation as the efficiency for electrons to pass these three cuts. It is identical for both electrons and positrons.

In order to determine the correction δ, a negative rigidity sample is selected for every cut using information from the detectors unrelated to that cut. The effects of the cut are compared between data and Monte Carlo simulation. This correction is found to be a smooth, slowly falling function of energy. It is -2% at 10 GeV and -6% at 700 GeV. The selection cut values and the identification cut values are chosen to maximize the measurement accuracy of the separate fluxes.

In each energy bin, a two-step fit procedure is performed to determine N_{e^+} and N_{e^-}. First, a *template* fit is used to find the number of electrons plus positrons reconstructed with a positive charge sign N^+ and the number of electrons plus positrons reconstructed with a negative charge sign N^-. The TRD templates, that is, the shapes of the TRD likelihood distributions for signal and background, are determined from data by selecting clean samples of electrons and protons using the ECAL estimator and the charge sign measured by the tracker. The TRD templates for electrons and positrons are identical. They are found to be independent of energy above 10 GeV. A maximum-likelihood fit of the resulting TRD templates to the data yields N^+, N^-, and the number of protons in the bin.

Second, N^+ and N^- are corrected for charge confusion. Charge confusion occurs when an electron is reconstructed as a positron and vice versa. There are two main sources of charge confusion. The first is related to the finite resolution of the tracker and multiple scattering. The second is related to the production of secondary tracks along the trajectory of the primary $e^{\pm}$. Charge confusion is determined using a dedicated estimator derived with a boosted decision tree technique which combines all the information from the tracker such as the track χ^2, the rigidity reconstructed using different sets of tracker layers, and the number of hits in the vicinity of the track. In each energy bin, two tracker templates are defined, one for particles with correctly reconstructed charge sign and another for particles with wrongly reconstructed charge sign. The former is defined using the negative rigidity data sample. The latter is based on the Monte Carlo simulation. These tracker templates are fit to data, bin by bin, to obtain the amount of charge confusion resulting in the determination of N_{e^+} and N_{e^-}.

In total, 9.23×10^6 events are identified as electrons and 0.58×10^6 as positrons. These numbers are slightly less than the numbers in our positron fraction publication [2] due to tighter selection criteria (such as on the exposure time) used to minimize the uncertainty of the separate flux measurements.

The systematic error associated with the uncertainty of the TRD template shapes for the signal and the background is due to the finite accuracy of the TRD alignment and calibration as well as to the statistics of the data samples used to construct the templates. This is the leading contribution to the total systematic error above 300 GeV.

The amount of charge confusion is well reproduced by the Monte Carlo simulation and a systematic uncertainty takes into account the small differences between data and the Monte Carlo simulation. This uncertainty is only significant for N_{e^+} in the highest energy bin.

The systematic error on the effective acceptance is given by the uncertainties on δ. For every cut, this uncertainty is derived from the comparison between data and the Monte Carlo simulation. This includes an overall scaling uncertainty of 2%, which introduces a correlation between energy bins and between the electron and positron fluxes. The acceptance uncertainty is the leading contribution to the systematic error below 300 GeV.

The total systematic error is taken as the quadratic sum of these three contributions and the minute bin-to-bin migration systematic. As an example, in the energy bin from 59.1 to 63.0 GeV, the statistical error on the positron flux is 4.9% and the total systematic error is 2.9% with 0.8% from the TRD templates, 0.4% from charge confusion, 2.8% from the effective acceptance, and 0.2% from bin-to-bin migration.

The complete analysis has been repeated 30 times with different sets of selection and identification cut values. All cuts have been varied in large ranges with the constraint that they lead, in combination, to a similar background rejection. The results of these analyses were found to be consistent. In addition, the time stability of the counting rates of $N_{e^{\pm}}$ has been studied. At high energies, all the rates are found to be stable, whereas at low energies, $\lesssim$10 GeV, variations with time are observed, as expected from solar modulation. Most importantly, several independent analyses were performed on the same data sample by different study groups. The results of those analyses are consistent with the results presented here.

Results.—The measured positron and electron fluxes are presented in Table I as a function of the energy at the top of AMS. The table also contains a representative value of the energy in the bin $\tilde{E}$ calculated according to Ref. [8] for a flux $\propto E^{-3}$ and the uncertainty on $\tilde{E}$.

The electron and positron fluxes multiplied by $\tilde{E}^3$ are presented in Fig. 1 together with the most recent measurements [9,10] for comparison. Figure 2 shows the detailed behavior for both electrons and positrons below 200 GeV together with previous measurements [9–14] in this energy range. Below ~10 GeV, the behavior for both electrons and

TABLE I. Results for the electron and positron fluxes according to Eq. (1) in units of $[\mathrm{m}^2\ \mathrm{sr\ s\ GeV}]^{-1}$. $\tilde{E}$ is as described in the text with its systematic error derived from the energy scale uncertainty. The bin boundaries and $\tilde{E}$ are the energies at the top of AMS. The systematic uncertainties include an overall scaling uncertainty of 2%, which introduces a correlation between energy bins and between the electron and positron fluxes.

Energy (GeV)	$\tilde{E}$ (GeV)	$\Phi_{e^-} \pm \sigma_{\mathrm{stat}} \pm \sigma_{\mathrm{syst}}$	$\Phi_{e^+} \pm \sigma_{\mathrm{stat}} \pm \sigma_{\mathrm{syst}}$
0.50–0.65	0.57 ± 0.03	$(1.47 \pm 0.03 \pm 0.16) \times 10^{1}$	$(1.31 \pm 0.20 \pm 0.23) \times 10^{0}$
0.65–0.82	0.73 ± 0.03	$(2.43 \pm 0.02 \pm 0.16) \times 10^{1}$	$(2.32 \pm 0.08 \pm 0.27) \times 10^{0}$
0.82–1.01	0.91 ± 0.04	$(2.08 \pm 0.01 \pm 0.14) \times 10^{1}$	$(1.91 \pm 0.04 \pm 0.15) \times 10^{0}$
1.01–1.22	1.11 ± 0.05	$(1.83 \pm 0.01 \pm 0.12) \times 10^{1}$	$(1.55 \pm 0.02 \pm 0.10) \times 10^{0}$
1.22–1.46	1.33 ± 0.05	$(1.64 \pm 0.00 \pm 0.09) \times 10^{1}$	$(1.34 \pm 0.01 \pm 0.08) \times 10^{0}$
1.46–1.72	1.58 ± 0.06	$(1.37 \pm 0.00 \pm 0.07) \times 10^{1}$	$(1.06 \pm 0.01 \pm 0.05) \times 10^{0}$
1.72–2.00	1.85 ± 0.07	$(1.11 \pm 0.00 \pm 0.05) \times 10^{1}$	$(8.01 \pm 0.05 \pm 0.38) \times 10^{-1}$
2.00–2.31	2.15 ± 0.08	$(8.94 \pm 0.01 \pm 0.40) \times 10^{0}$	$(6.19 \pm 0.04 \pm 0.28) \times 10^{-1}$
2.31–2.65	2.47 ± 0.08	$(7.10 \pm 0.01 \pm 0.30) \times 10^{0}$	$(4.59 \pm 0.03 \pm 0.19) \times 10^{-1}$
2.65–3.00	2.82 ± 0.09	$(5.49 \pm 0.01 \pm 0.22) \times 10^{0}$	$(3.43 \pm 0.02 \pm 0.14) \times 10^{-1}$
3.00–3.36	3.17 ± 0.10	$(4.61 \pm 0.01 \pm 0.17) \times 10^{0}$	$(2.78 \pm 0.02 \pm 0.11) \times 10^{-1}$
3.36–3.73	3.54 ± 0.11	$(3.62 \pm 0.01 \pm 0.13) \times 10^{0}$	$(2.12 \pm 0.01 \pm 0.08) \times 10^{-1}$
3.73–4.12	3.92 ± 0.12	$(2.87 \pm 0.00 \pm 0.10) \times 10^{0}$	$(1.64 \pm 0.01 \pm 0.06) \times 10^{-1}$
4.12–4.54	4.32 ± 0.12	$(2.27 \pm 0.00 \pm 0.08) \times 10^{0}$	$(1.28 \pm 0.01 \pm 0.04) \times 10^{-1}$
4.54–5.00	4.76 ± 0.13	$(1.80 \pm 0.00 \pm 0.06) \times 10^{0}$	$(9.86 \pm 0.07 \pm 0.32) \times 10^{-2}$
5.00–5.49	5.24 ± 0.14	$(1.42 \pm 0.00 \pm 0.04) \times 10^{0}$	$(7.76 \pm 0.05 \pm 0.24) \times 10^{-2}$
5.49–6.00	5.74 ± 0.15	$(1.11 \pm 0.00 \pm 0.03) \times 10^{0}$	$(5.94 \pm 0.04 \pm 0.18) \times 10^{-2}$
6.00–6.54	6.26 ± 0.15	$(8.80 \pm 0.01 \pm 0.25) \times 10^{-1}$	$(4.69 \pm 0.04 \pm 0.14) \times 10^{-2}$
6.54–7.10	6.81 ± 0.16	$(6.95 \pm 0.01 \pm 0.20) \times 10^{-1}$	$(3.74 \pm 0.03 \pm 0.11) \times 10^{-2}$
7.10–7.69	7.39 ± 0.17	$(5.51 \pm 0.01 \pm 0.15) \times 10^{-1}$	$(2.94 \pm 0.02 \pm 0.09) \times 10^{-2}$
7.69–8.30	7.99 ± 0.18	$(4.36 \pm 0.01 \pm 0.12) \times 10^{-1}$	$(2.34 \pm 0.02 \pm 0.07) \times 10^{-2}$
8.30–8.95	8.62 ± 0.19	$(3.50 \pm 0.01 \pm 0.10) \times 10^{-1}$	$(1.91 \pm 0.02 \pm 0.05) \times 10^{-2}$
8.95–9.62	9.28 ± 0.19	$(2.78 \pm 0.01 \pm 0.08) \times 10^{-1}$	$(1.50 \pm 0.02 \pm 0.04) \times 10^{-2}$
9.62–10.3	9.96 ± 0.20	$(2.24 \pm 0.01 \pm 0.06) \times 10^{-1}$	$(1.25 \pm 0.01 \pm 0.04) \times 10^{-2}$
10.3–11.0	10.7 ± 0.2	$(1.79 \pm 0.00 \pm 0.04) \times 10^{-1}$	$(1.01 \pm 0.01 \pm 0.03) \times 10^{-2}$
11.0–11.8	11.4 ± 0.2	$(1.47 \pm 0.00 \pm 0.03) \times 10^{-1}$	$(8.30 \pm 0.10 \pm 0.21) \times 10^{-3}$
11.8–12.6	12.2 ± 0.2	$(1.19 \pm 0.00 \pm 0.03) \times 10^{-1}$	$(6.81 \pm 0.09 \pm 0.17) \times 10^{-3}$
12.6–13.4	13.0 ± 0.3	$(9.73 \pm 0.03 \pm 0.23) \times 10^{-2}$	$(5.76 \pm 0.08 \pm 0.14) \times 10^{-3}$
13.4–14.2	13.8 ± 0.3	$(7.97 \pm 0.03 \pm 0.19) \times 10^{-2}$	$(4.60 \pm 0.07 \pm 0.11) \times 10^{-3}$
14.2–15.1	14.7 ± 0.3	$(6.56 \pm 0.02 \pm 0.15) \times 10^{-2}$	$(3.84 \pm 0.06 \pm 0.09) \times 10^{-3}$
15.1–16.1	15.6 ± 0.3	$(5.39 \pm 0.02 \pm 0.13) \times 10^{-2}$	$(3.33 \pm 0.05 \pm 0.08) \times 10^{-3}$
16.1–17.0	16.5 ± 0.3	$(4.48 \pm 0.02 \pm 0.11) \times 10^{-2}$	$(2.81 \pm 0.05 \pm 0.07) \times 10^{-3}$
17.0–18.0	17.5 ± 0.3	$(3.71 \pm 0.02 \pm 0.09) \times 10^{-2}$	$(2.37 \pm 0.04 \pm 0.06) \times 10^{-3}$
18.0–19.0	18.5 ± 0.4	$(3.10 \pm 0.01 \pm 0.07) \times 10^{-2}$	$(2.01 \pm 0.04 \pm 0.05) \times 10^{-3}$
19.0–20.0	19.5 ± 0.4	$(2.59 \pm 0.01 \pm 0.06) \times 10^{-2}$	$(1.74 \pm 0.03 \pm 0.04) \times 10^{-3}$
20.0–21.1	20.6 ± 0.4	$(2.17 \pm 0.01 \pm 0.05) \times 10^{-2}$	$(1.44 \pm 0.03 \pm 0.04) \times 10^{-3}$
21.1–22.2	21.7 ± 0.4	$(1.82 \pm 0.01 \pm 0.04) \times 10^{-2}$	$(1.22 \pm 0.03 \pm 0.03) \times 10^{-3}$
22.2–23.4	22.8 ± 0.5	$(1.56 \pm 0.01 \pm 0.04) \times 10^{-2}$	$(1.05 \pm 0.02 \pm 0.03) \times 10^{-3}$
23.4–24.6	24.0 ± 0.5	$(1.31 \pm 0.01 \pm 0.03) \times 10^{-2}$	$(9.33 \pm 0.22 \pm 0.23) \times 10^{-4}$
24.6–25.9	25.2 ± 0.5	$(1.11 \pm 0.01 \pm 0.03) \times 10^{-2}$	$(7.88 \pm 0.19 \pm 0.20) \times 10^{-4}$
25.9–27.2	26.6 ± 0.5	$(9.42 \pm 0.06 \pm 0.23) \times 10^{-3}$	$(6.63 \pm 0.17 \pm 0.17) \times 10^{-4}$
27.2–28.7	28.0 ± 0.6	$(7.94 \pm 0.05 \pm 0.20) \times 10^{-3}$	$(5.94 \pm 0.16 \pm 0.15) \times 10^{-4}$
28.7–30.2	29.4 ± 0.6	$(6.74 \pm 0.05 \pm 0.17) \times 10^{-3}$	$(5.20 \pm 0.14 \pm 0.13) \times 10^{-4}$
30.2–31.8	31.0 ± 0.6	$(5.62 \pm 0.04 \pm 0.14) \times 10^{-3}$	$(4.33 \pm 0.12 \pm 0.11) \times 10^{-4}$
31.8–33.5	32.7 ± 0.7	$(4.73 \pm 0.04 \pm 0.12) \times 10^{-3}$	$(3.76 \pm 0.11 \pm 0.10) \times 10^{-4}$
33.5–35.4	34.4 ± 0.7	$(3.92 \pm 0.03 \pm 0.10) \times 10^{-3}$	$(3.20 \pm 0.10 \pm 0.08) \times 10^{-4}$
35.4–37.3	36.3 ± 0.7	$(3.37 \pm 0.03 \pm 0.09) \times 10^{-3}$	$(2.69 \pm 0.09 \pm 0.07) \times 10^{-4}$
37.3–39.4	38.3 ± 0.8	$(2.83 \pm 0.03 \pm 0.07) \times 10^{-3}$	$(2.43 \pm 0.08 \pm 0.07) \times 10^{-4}$
39.4–41.6	40.5 ± 0.8	$(2.34 \pm 0.02 \pm 0.06) \times 10^{-3}$	$(2.11 \pm 0.07 \pm 0.06) \times 10^{-4}$
41.6–44.0	42.8 ± 0.9	$(2.01 \pm 0.02 \pm 0.05) \times 10^{-3}$	$(1.70 \pm 0.06 \pm 0.05) \times 10^{-4}$
44.0–46.6	45.3 ± 0.9	$(1.63 \pm 0.02 \pm 0.04) \times 10^{-3}$	$(1.56 \pm 0.06 \pm 0.04) \times 10^{-4}$
46.6–49.3	47.9 ± 1.0	$(1.38 \pm 0.02 \pm 0.04) \times 10^{-3}$	$(1.22 \pm 0.05 \pm 0.03) \times 10^{-4}$
49.3–52.3	50.8 ± 1.0	$(1.14 \pm 0.01 \pm 0.03) \times 10^{-3}$	$(1.08 \pm 0.05 \pm 0.03) \times 10^{-4}$

(Table continued)

TABLE I. (*Continued*)

Energy (GeV)	$\tilde{E}$ (GeV)	$\Phi_{e^-} \pm \sigma_{\text{stat}} \pm \sigma_{\text{syst}}$	$\Phi_{e^+} \pm \sigma_{\text{stat}} \pm \sigma_{\text{syst}}$
52.3–55.6	53.9 ± 1.1	$(9.35 \pm 0.12 \pm 0.26) \times 10^{-4}$	$(9.37 \pm 0.42 \pm 0.27) \times 10^{-5}$
55.6–59.1	57.3 ± 1.1	$(7.61 \pm 0.10 \pm 0.21) \times 10^{-4}$	$(7.55 \pm 0.36 \pm 0.22) \times 10^{-5}$
59.1–63.0	61.0 ± 1.2	$(6.32 \pm 0.09 \pm 0.18) \times 10^{-4}$	$(6.53 \pm 0.32 \pm 0.19) \times 10^{-5}$
63.0–67.3	65.1 ± 1.3	$(5.05 \pm 0.08 \pm 0.14) \times 10^{-4}$	$(5.41 \pm 0.28 \pm 0.16) \times 10^{-5}$
67.3–72.0	69.6 ± 1.4	$(3.92 \pm 0.07 \pm 0.11) \times 10^{-4}$	$(4.78 \pm 0.25 \pm 0.14) \times 10^{-5}$
72.0–77.4	74.6 ± 1.5	$(3.26 \pm 0.06 \pm 0.10) \times 10^{-4}$	$(3.89 \pm 0.21 \pm 0.12) \times 10^{-5}$
77.4–83.4	80.3 ± 1.6	$(2.54 \pm 0.05 \pm 0.08) \times 10^{-4}$	$(2.88 \pm 0.17 \pm 0.09) \times 10^{-5}$
83.4–90.2	86.7 ± 1.7	$(2.03 \pm 0.04 \pm 0.06) \times 10^{-4}$	$(2.76 \pm 0.16 \pm 0.09) \times 10^{-5}$
90.2–98.1	94.0 ± 1.9	$(1.56 \pm 0.03 \pm 0.05) \times 10^{-4}$	$(2.08 \pm 0.13 \pm 0.07) \times 10^{-5}$
98.1–107	103 ± 2	$(1.23 \pm 0.03 \pm 0.04) \times 10^{-4}$	$(1.53 \pm 0.10 \pm 0.06) \times 10^{-5}$
107–118	113 ± 2	$(9.02 \pm 0.21 \pm 0.31) \times 10^{-5}$	$(1.15 \pm 0.08 \pm 0.04) \times 10^{-5}$
118–132	125 ± 3	$(6.59 \pm 0.16 \pm 0.23) \times 10^{-5}$	$(8.56 \pm 0.66 \pm 0.33) \times 10^{-6}$
132–149	140 ± 3	$(4.32 \pm 0.12 \pm 0.16) \times 10^{-5}$	$(6.21 \pm 0.53 \pm 0.25) \times 10^{-6}$
149–170	159 ± 3	$(3.02 \pm 0.09 \pm 0.11) \times 10^{-5}$	$(5.23 \pm 0.45 \pm 0.22) \times 10^{-6}$
170–198	183 ± 4	$(1.93 \pm 0.07 \pm 0.07) \times 10^{-5}$	$(3.19 \pm 0.32 \pm 0.14) \times 10^{-6}$
198–237	216 ± 4	$(1.11 \pm 0.04 \pm 0.05) \times 10^{-5}$	$(2.08 \pm 0.23 \pm 0.10) \times 10^{-6}$
237–290	262 ± 5	$(6.64 \pm 0.31 \pm 0.31) \times 10^{-6}$	$(1.21 \pm 0.17 \pm 0.07) \times 10^{-6}$
290–370	327 ± 7	$(3.15 \pm 0.19 \pm 0.19) \times 10^{-6}$	$(6.17 \pm 1.20 \pm 0.38) \times 10^{-7}$
370–500	429 ± 13	$(1.21 \pm 0.10 \pm 0.09) \times 10^{-6}$	$(2.47 \pm 0.73 \pm 0.22) \times 10^{-7}$
500–700	589 ± 22	$(4.53 \pm 0.64 \pm 0.70) \times 10^{-7}$	

positrons is affected by solar modulation as seen in our data by variations of the fluxes over this data-taking interval. However, above ~20 GeV the effects of solar modulation are insignificant within the current experimental accuracy. The data show that above ~20 GeV and up to 200 GeV the electron flux decreases more rapidly with energy than the positron flux, that is, the electron flux is softer than the positron flux. This is not consistent with only the secondary production of positrons [15].

As seen in Figs. 1 and 2, neither the electron flux nor the positron flux can be described by single power laws ($\propto E^{\gamma}$) over the entire range. To estimate a lower energy limit above which a single power law describes the positron flux, we use energy intervals with starting energies from 0.5 GeV and increasing bin by bin. The ending energy for all intervals is fixed at 500 GeV. Each interval is split into two sections with a boundary between the starting energy and 500 GeV. Each of the two sections is fit with a single power law and we obtain two spectral indices. The lowest starting energy of the interval that gives consistent spectral indices at the 90% C.L. for any boundary defines the lower limit. This yields 27.2 GeV for positrons. Similarly, starting from 0.5 GeV and ending at 700 GeV yields a lower limit of 52.3 GeV for electrons.

To quantitatively examine the energy dependence of the fluxes in a model-independent way, each of them is fit with a spectral index $\gamma_{e^{\pm}}$ as

$$\Phi_{e^{\pm}}(E) = C_{e^{\pm}} E^{\gamma_{e^{\pm}}} \quad \text{or} \quad \gamma_{e^{\pm}} = d[\log(\Phi_{e^{\pm}})]/d[\log(E)] \tag{3}$$

(E in GeV and $C_{e^{\pm}}$ are normalizations) over a sliding energy window, where the width of the window varies with energy to have sufficient sensitivity to determine the spectral index. The resulting energy dependencies of the fitted spectral indices are shown in Fig. 3, where the shading indicates the correlation between neighboring points due to the sliding energy window. The steep softening of the spectral indices below 10 GeV is due to solar modulation. Above 20 GeV, that is, above the effects of solar modulation, the spectral indices for positrons and electrons are significantly different. From 20 to 200 GeV, γ_{e^+} is significantly harder than γ_{e^-}. This demonstrates that the increase with energy observed in the positron fraction is due to the hardening of positron spectrum and not to the softening of the electron spectrum above 10 GeV.

Figure 3 indicates the possible existence of structures in γ_{e^+} and γ_{e^-}. Explicitly, single power-law fits over different energy ranges show that γ_{e^+} hardens from -2.97 ± 0.03 (fit over 15.1–31.8 GeV) to -2.75 ± 0.05 (fit over 49.3–198 GeV). Correspondingly, γ_{e^-} hardens from -3.28 ± 0.03 (fit over 19.0–31.8 GeV) to -3.15 ± 0.04 (fit over 83.4–290 GeV) and then levels off. Note that the quoted values of the spectral indices correspond to fits from nonoverlapping ranges and are not correlated. Above ~200 GeV, γ_{e^+} exhibits a tendency to soften with energy. This is consistent with our observation in Ref. [2] that above ~200 GeV the positron fraction is no longer increasing with energy.

These measurements of the electron flux and positron flux make possible the accurate comparison with various

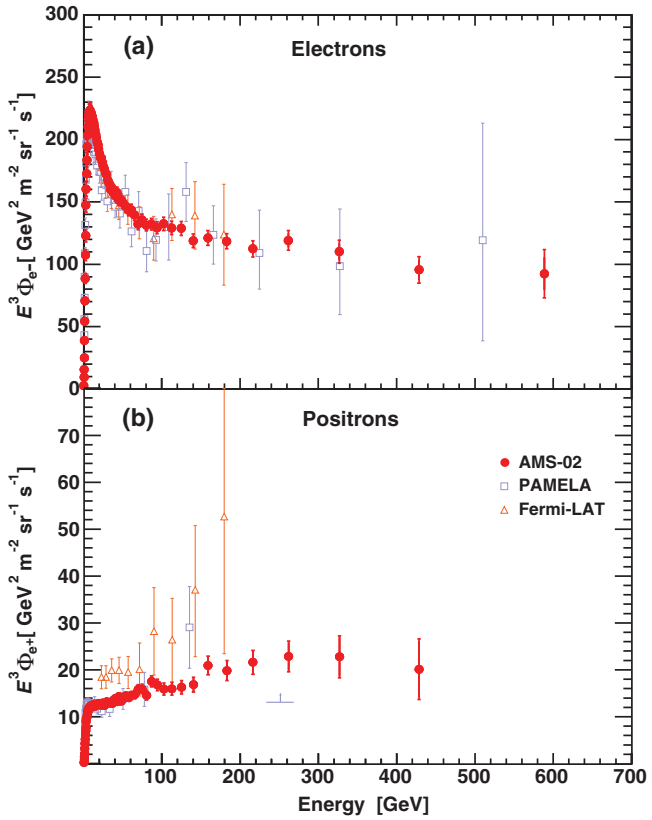

FIG. 1 (color). The AMS (a) electron and (b) positron fluxes, multiplied by $\tilde{E}^3$. Statistical and systematic uncertainties of the AMS results have been added in quadrature. Also shown are the most recent measurements from PAMELA [9] and Fermi-LAT [10].

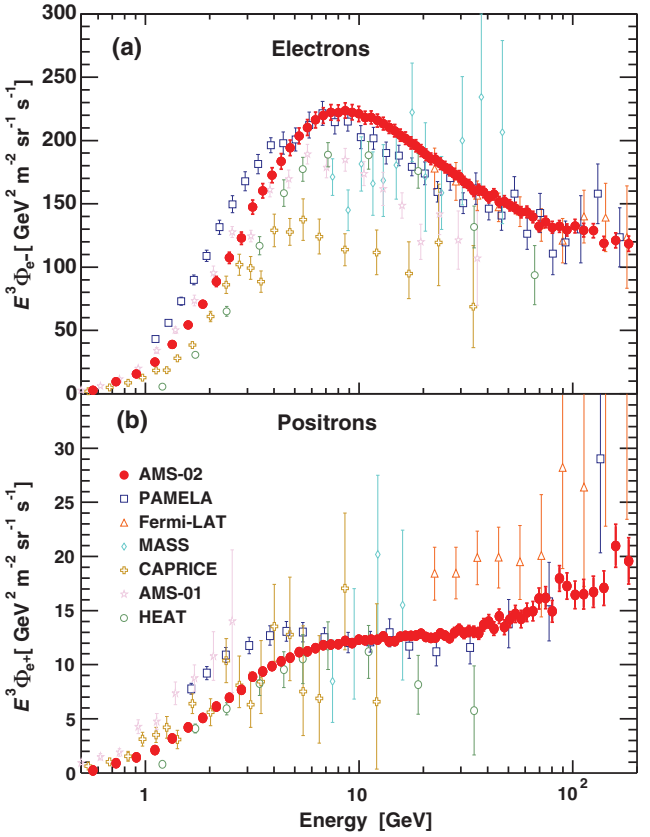

FIG. 2 (color). Detailed AMS (a) electron and (b) positron fluxes, multiplied by $\tilde{E}^3$, up to 200 GeV, with earlier measurements by PAMELA [9], Fermi-LAT [10], MASS [11], CAPRICE [12], AMS-01 [13], and HEAT [14].

astrophysical models including the minimal model discussed in Refs. [1,2]. This will be presented in a separate publication.

The differing behavior of the spectral indices versus energy indicates that high-energy positrons have a different origin from that of electrons. The underlying mechanism of this behavior can only be ascertained by continuing to collect data up to the TeV region (currently, the largest uncertainties above ~200 GeV are the statistical errors) and by measuring the antiproton to proton ratio to high energies. These are among the main goals of AMS.

In conclusion, the electron flux and the positron flux each require a description beyond a single power-law spectrum. Both the electron flux and the positron flux change their behavior at ~30 GeV, but the fluxes are significantly different in their magnitude and energy dependence. Between 20 and 200 GeV, the positron spectral index is significantly harder than the electron spectral index. These precise measurements show that the rise in the positron fraction is due to the hardening of the positron spectrum and not to the softening of the electron spectrum above 10 GeV. The determination of the differing behavior of the spectral indices versus energy is a new observation and provides important information on the origins of cosmic-ray electrons and positrons.

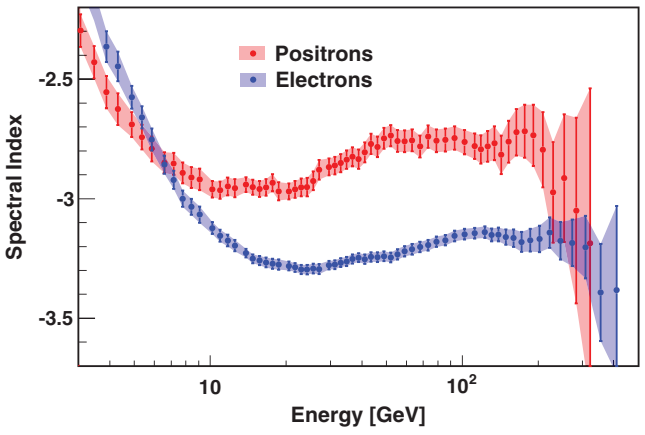

FIG. 3 (color). The spectral indices of the electron flux γ_{e^-} and of the positron flux γ_{e^+} as a function of energy. The shaded regions indicate the 68% C.L. intervals including the correlation between neighboring points due to the sliding energy window.

We thank former NASA Administrator Daniel S. Goldin for his dedication to the legacy of the ISS as a scientific laboratory and his decision for NASA to fly AMS as a DOE payload. We also acknowledge the support of the NASA leadership including Charles Bolden and William Gerstenmeier. We are grateful for the support of Jim Siegrist and Michael Salamon of the DOE. We also acknowledge the continuous support from MIT and its School of Science, Michael Sipser, Marc Kastner, Ernest Moniz, and Richard Milner. We acknowledge support from CAS, NNSF, MOST, NLAA, and the provincial governments of Shandong, Jiangsu, and Guangdong, China; CNRS, IN2P3, CNES, Enigmass, and the ANR, France; J. Trümper, J. D. Woerner, and DLR, Germany; INFN and ASI, Italy; CIEMAT, CDTI, SEIDI–MINECO, and CPAN, Spain; the Swiss National Science Foundation (SNSF), federal and cantonal authorities, Switzerland; and Academia Sinica and the National Science Council (NSC), former President of Academia Sinica Yuan-Tseh Lee, and former Ministers of NSC, Maw-Kuen Wu and Luo-Chuan Lee, Taiwan. We gratefully acknowledge the strong support from CERN, including Rolf-Dieter Heuer, and ESA. We are grateful for important discussions with Barry Barish, Jonathan Ellis, Neal Lane, Steve Olsen, Álvaro de Rújula, George Smoot, Steven Weinberg, and Frank Wilczek. The strong support of the flight control teams at JSC and MSFC has allowed AMS to operate optimally on the ISS for over three years. The work of J. Bazo, F. Nozzoli, and C. Pizzolotto was carried out at the ASI Science Data Center (ASDC) in the framework of ASI-INFN Agreement No. C/011/11/1. M. Vecchi is supported by the Centre national d'études spatiales, CNES. Work at Aachen University is supported by the Deutsches Zentrum für Luft- und Raumfahrt, DLR, and computing resources from JARA-HPC under Project No. JARA0052. Work at METU is supported by the Turkish Atomic Energy Authority, TAEK. Work at IHEP is supported by the National Natural Science Foundation of China. Work at INFN-Sezione di Bologna, INFN-Sezione di Milano, INFN-Sezione di Perugia, INFN-Sezione di Pisa, INFN—TIFPA, and Universit'a di Trento, INFN-Sezione di Roma is supported by the Italian Space Agency, ASI, Contract No. ASI-INFN I/002/13/0. Both NCU and the Institute of Physics, Academia Sinica, are supported by the Ministry of Science and Technology. Work at CHEP, Kyungpook National University is supported by Grants No. NRF-2009-0080142 and No. NRF-2012-010226. We acknowledge computing resources from JARA-HPC under Project No. JARA0052. Institut für Experimentelle Kernphysik is supported by the Deutsches Zentrum für Luft- und Raumfahrt, DLR. Work at CIEMAT is also supported by SEIDI and CPAN. Work at UNAM is supported by Consejo Nacional de Ciencia y Tecnología, CONACYT. Work at Ewha Womans University is supported by Grant No. NRF-2013-004883. This work was supported by the China Scholarship Council.

[*]Deceased.
[†]Current address: ISDC, CH-1290 Versoix, Switzerland.
[‡]Also at ASI, Rome I-00133, Italy.
[§]Also at Xi'an Jiaotong University, XJTU, Xi'an 710049, China.
[‖]Also at Sun Yat-Sen University, SYSU, Guangzhou 510275, China.
[¶]Current address: European Organization for Nuclear Research, CERN, CH-1211 Geneva 23, Switzerland.
[**]Also at Shandong University, SDU, Jinan, Shandong 250100, China.
[††]Also at Harbin Institute of Technology, HIT, Harbin 150001, China.
[‡‡]Also at University of Science and Technology of China, USTC, Hefei, 230026, China.
[§§]Also at Università di Siena, I-53100 Siena, Italy.
[‖‖]Also at Beijing Normal University, BNU, Beijing 100875, China.
[¶¶]Also at Southeast University, SEU, Nanjing 210096, China.

[1] M. Aguilar *et al.*, Phys. Rev. Lett. **110**, 141102 (2013).
[2] L. Accardo *et al.*, preceding Letter, Phys. Rev. Lett. **113**, 121101 (2014).
[3] L. Feng, R.-Z. Yang, H.-N. He, T.-K. Dong, Y.-Z. Fan, and J. Chang, Phys. Lett. B **728**, 250 (2014); K. Blum, B. Katz, and E. Waxman, Phys. Rev. Lett. **111**, 211101 (2013); L. Bergström, T. Bringmann, I. Cholis, D. Hooper, and C. Weniger, Phys. Rev. Lett. **111**, 171101 (2013); I. Cholis and D. Hooper, Phys. Rev. D **88**, 023013 (2013); T. Linden and S. Profumo, Astrophys. J. **772**, 18 (2013).
[4] A. Kounine, Int. J. Mod. Phys. E **21**, 1230005 (2012); S. C. C. Ting, in *Proceedings of 4th International Conference on Particle and Fundamental Physics in Space (NUPHPB)* (unpublished); S. C. Lee, in *Proceedings of the 20th International Conference on Supersymmetry and Unification of Fundamental Interactions, Beijing, 2012* (unpublished); M. Aguilar, in *Proceedings of the XL International Meeting on Fundamental Physics, Centro de Ciencias de Benasque Pedro Pascual, 2012* (unpublished); S. Schael, in *Proceedings of the 10th Symposium on Sources and Detection of Dark Matter and Dark Energy in the Universe, Los Angeles, 2012* (unpublished); B. Bertucci, *Proc. Sci.*, EPS-HEP (2011) 67; M. Incagli, AIP Conf. Proc. **1223**, 43 (2009); R. Battiston, Nucl. Instrum. Methods Phys. Res., Sect. A **588**, 227 (2008).
[5] B. P. Roe, H.-J. Yang, J. Zhu, Y. Liu, I. Stancu, and G. McGregor, Nucl. Instrum. Methods Phys. Res., Sect. A **543**, 577 (2005).
[6] J. Allison *et al.*, IEEE Trans. Nucl. Sci. **53**, 270 (2006); S. Agostinelli *et al.*, Nucl. Instrum. Methods Phys. Res., Sect. A **506**, 250 (2003).
[7] C. Størmer, *The Polar Aurora* (Oxford University Press, London, 1950).
[8] G. D. Lafferty and T. R. Wyatt, Nucl. Instrum. Methods Phys. Res., Sect. A **355**, 541 (1995). We have used Eq. (6) to obtain $\tilde{\boldsymbol{E}}$ with $\tilde{\boldsymbol{E}} = \boldsymbol{x}_{lw}$.
[9] O. Adriani *et al.*, Phys. Rev. Lett. **111**, 081102 (2013); O. Adriani *et al.*, Phys. Rev. Lett. **106**, 201101 (2011).
[10] M. Ackermann *et al.*, Phys. Rev. Lett. **108**, 011103 (2012).
[11] C. Grimani *et al.*, Astron. Astrophys. **392**, 287 (2002).

[12] M. Boezio *et al.*, Astrophys. J. **532**, 653 (2000).
[13] M. Aguilar *et al.*, Phys. Lett. B **484**, 10 (2000).
[14] M. A. DuVernois *et al.*, Astrophys. J. **559**, 296 (2001).
[15] P. D. Serpico, Astropart. Phys. **39–40**, 2 (2012); T. Delahaye, R. Lineros, F. Donato, N. Fornengo, J. Lavalle, P. Salati, and R. Taillet, Astron. Astrophys. **501**, 821 (2009); I. V. Moskalenko and A. W. Strong, Astrophys. J. **493**, 694 (1998). We have not included the model predictions as their uncertainty, $\mathcal{O}(20\%)$, is larger than our errors; I. V. Moskalenko (private communication).